The Astrophysical Journal, 1003:207 (11pp), 2026 June 1 https://doi.org/10.3847/1538-4357/ae6589

The 3He-rich SEP on Event 2024 April 1 at 27 Solar Radii—Indications of Acceleration by Waves and Implications of Coronal Source Location

D. G. Mitchell[1], D. Lario[2], N. E. Raouafi[1], G. M. Mason[1], A. Kouloumvakos[1], H. Collier[3,4], E. C. Roelof[1], G. Berland[1], D. J. McComas[5], C. M. S. Cohen[6], M. E. Hill[1], R. L. McNutt, Jr[1], P. S. Mostafavi[1], J. C. Kasper[7], S. D. Bale[8], M. Pulupa[8], and P. L. Whittlesey[8]
[1] Johns Hopkins Applied Physics Laboratory, Laurel, MD 20723, USA; don.mitchell@jhuapl.edu
[2] Heliophysics Science Division, NASA Goddard Space Flight Center, Greenbelt, MD 20771, USA
[3] University of Applied Sciences and Arts Northwestern Switzerland (FHNW), Bahnhofstrasse 6, 5210 Windisch, Switzerland
[4] ETH Zürich in collaboration with the University of Applied Science and Arts, Northwestern, Switzerland
[5] Department of Astrophysical Sciences, Princeton University, Princeton, NJ 08544, USA
[6] California Institute of Technology, Pasadena, CA 91125, USA
[7] University of Michigan, Ann Arbor, MI 48109, USA
[8] University of California at Berkeley, Berkeley, CA 94720, USA
Received 2025 May 31; revised 2026 April 17; accepted 2026 April 18; published 2026 May 26

Abstract

Parker Solar Probe (PSP) observations of a small dispersive event on 2024 April 1 reveal highly enriched ^{3}He abundance in the suprathermal energy range (40–250 keV nucleon^{-1}). Time dispersion observed in this impulsive solar energetic particle (SEP) event is consistent with an estimated onset time of 22:50 UT on 2024 March 31. The event occurred during an orbital segment as PSP moved from about 27 R_s to about 29 R_s while outbound in orbit 19. For this segment of the orbit, PSP's motion in Carrington coordinates remains within about 1° of the same Carrington longitude. The ^{3}He content is much larger than the usual SEP abundances, especially in this energy range. Additionally, the ^{3}He energy spectrum is not power law in shape, unlike the H and ^{4}He spectra. Heavy ions (O, Fe) are also somewhat enhanced. These compositional signatures suggest that this is an example of resonant wave–particle acceleration, as hypothesized for generating the suprathermal seed particles required to account for the enrichment of various species above solar abundances in shock (or compression) acceleration models of SEP events. Like many previously reported impulsive ^{3}He-rich events, this event is associated with an energetic electron beam, type III radio emission, and a hard X-ray flare. However, associating the hard X-ray event with this SEP event requires significant (∼60°) prompt longitudinal propagation of energetic particles in the low corona before they access open magnetic flux, complicating its interpretation as part of the source process for this particular event.

Unified Astronomy Thesaurus concepts: Solar energetic particles (1491); Solar particle emission (1517); Solar active region magnetic fields (1975)

1. Introduction

Solar energetic particle (SEP) events observed in interplanetary space have been associated with both flares and coronal mass ejections (CMEs). Most SEP observations have been made from ∼1 au, a fact that automatically selects for large events. Reconnection, shocks, and compressions are generally invoked to explain the energetic ion and electron populations. Reconnection is usually associated with the acceleration of particles in solar flares (e.g., V. V. Zharkova et al. 2011), whereas diffusive shock acceleration is typically invoked for the case of CME-driven shocks (D. V. Reames 1999). In the low corona, compressions may also serve as significant accelerators even before shocks fully develop (N. A. Schwadron et al. 2015). To address the frequently observed enhanced abundances of ^{3}He and heavy ions in many such events (particularly those associated with shocks or compressions), wave–particle heating and acceleration have long been considered as likely precursors that selectively seed the plasma with ^{3}He- and heavy-ion-enriched suprathermal ions prior to subsequent shock and/or compression wave acceleration.

As discussed by D. G. Mitchell et al. (2024), energetic-particle seed populations accompanied by nearly scatter-free electrons and species such as ^{3}He are known to be associated with flares (G. M. Mason et al. 1986, 2002, 2009, 2023; D. V. Reames 1999, 2024; M. I. Desai et al. 2003). A key question remains as to how exactly suprathermal particle seed populations are generated to begin with. Data from the Energetic Particle Instruments (EPIs) of the Integrated Science Investigation of the Sun (IS⊙IS; D. J. McComas et al. 2016) on board the Parker Solar Probe (PSP; Fox et al. 2016), especially when close to the Sun, provide an opportunity to measure relatively small and isolated SEP events that are uncomplicated by shocks or compressions and may still bear the imprint of mechanisms for the generation of these seed particles.

One mechanism invoked in an attempt to account for events with enhanced ^{3}He/^{4}He ratios involves resonant acceleration by waves, the latter generated by outward-streaming beams of energetic electrons (M. Temerin & I. Roth 1992; I. Roth & M. Temerin 1997). This mechanism, though referred to in more recent literature (e.g., D. V. Reames 2015), has not gained broad acceptance because of its perceived deficiencies

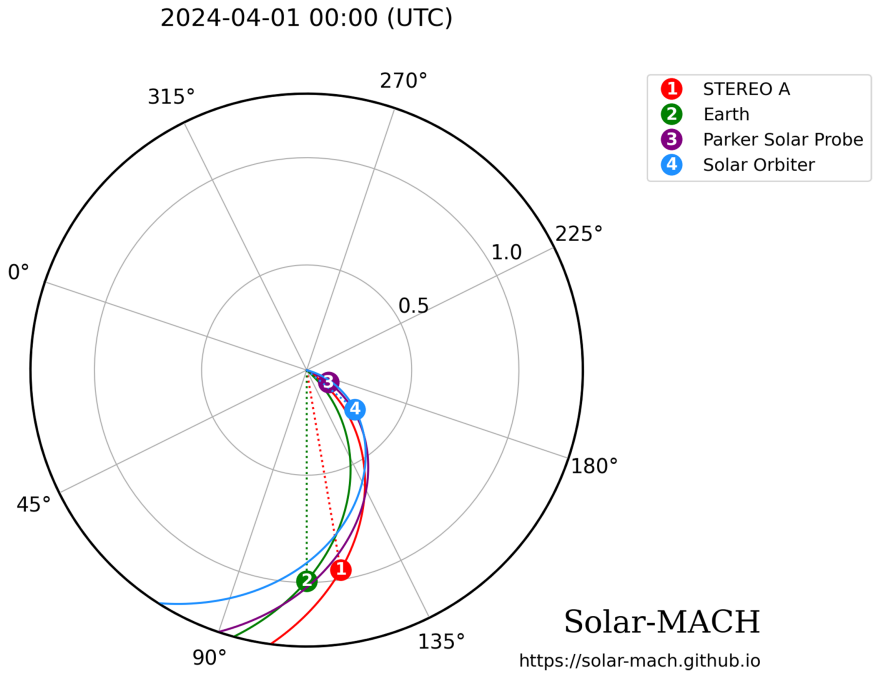

Figure 1. Diagram of the loci of STEREO-A, Earth, Parker Solar Probe, and Solar Orbiter at the beginning of 2024 April 1, provided by the Solar MACH application (https://solar-mach.streamlit.app/; J. Gieseler et al. 2023). All four vantage points lie on Parker-spiral traces connected to closely adjacent high-coronal footpoint longitudes.

in explaining the associated heavy-ion enrichment in ^{3}He-rich events. D. G. Mitchell et al. (2020) argue that the perceived deficiencies can be overcome and suggest that current instabilities, combined with parallel electric fields (perhaps associated with reconnection), can generate seed populations enriched within particular charge-to-mass ratio ranges, depending on the wave-power frequency distribution. G. M. Mason et al. (2023) show strong evidence for wave–particle heating across nearly all ion species, except for those with $M/q = 1$ and 2, where the wave power at frequencies resonant with H and ^{4}He is reduced, presumably quenched by the relatively high densities of these major species in the low corona.

The small event observed by PSP on 2024 April 1 stands out both for its clear dispersion (indicating near scatter-free transport from its coronal source), and for its uniquely high ^{3}He content (the highest ^{3}He/^{4}He ratio observed by PSP in the 40–250 keV amu^{-1} energy range). It may be that both features are a consequence of reconnection combined with wave–particle heating at the source. Only a small subset of jets or jetlets suggested by N. E. Raouafi et al. (2023) as the sources of the solar wind are thought likely to produce transient SEP events such as the one seen here. Ubiquitous small-scale magnetic reconnection processes generate tiny jets of hot plasma, known as jetlets (N. E. Raouafi & G. Stenborg 2014). N. E. Raouafi et al. (2023) argued that these jetlets are the source of both regimes of the solar wind. S. D. Bale et al. (2023) proposed a model for the acceleration of solar wind in the low corona through reconnection between open magnetic field and closed loops. This model also results in a power-law tail in the energetic-particle distributions (protons and helium in the test cases), which may account for the transient energetic-particle events seen, especially close to the Sun.

2. SEP Event of 2024 March 31–April 1

On 2024 April 1, PSP was outbound at a distance of about 27 R_s from the Sun, a part of its orbit where its connection longitude remains nearly fixed as the PSP azimuthal motion matches the Sun's angular rotation. The Parker spiral mapping of PSP to the high corona is represented in Figure 1, which also shows the close nominal magnetic alignment of Earth, STEREO-A, and Solar Orbiter (SO) along Parker-spiral field lines connected to similar high-coronal longitudes. These calculated magnetic connection points are approximate and subject to solar wind speed, the assumed coronal altitude at which the solar wind becomes radial, and assumptions regarding a parallel current-free corona. As we will elaborate later in this paper, these connection points are useful for establishing that PSP and SO map to similar locations in the high corona. Just how similar, and how high in the corona, remains open to interpretation.

Figure 2 presents an overview of the event. Although Figure 1 shows that multiple spacecraft were magnetically connected to the same general coronal longitude, the event was only detected by PSP. At about 23:40 UT on 2024 March 31, energetic particles were first observed by the IS⊙IS EPI-Lo sensor (D. J. McComas et al. 2016; M. E. Hill et al. 2017), primarily in the sunward-facing apertures of the 80 aperture sensor. EPI-Lo measured ^{4}He up to a total energy of ∼1 MeV, with lower-energy particles following in a typical time-dispersed sequence characteristic of sudden-onset SEP events. EPI-Lo also measured the dispersive event in protons (near the lower limit of the EPI-Lo energy range, ∼80–200 keV, such that the dispersion was less clearly seen), as well as in ^{3}He, O, and Fe. The event time history is most clearly seen in the ^{4}He and ^{3}He data, a consequence of their relatively high detection efficiency in EPI-Lo.

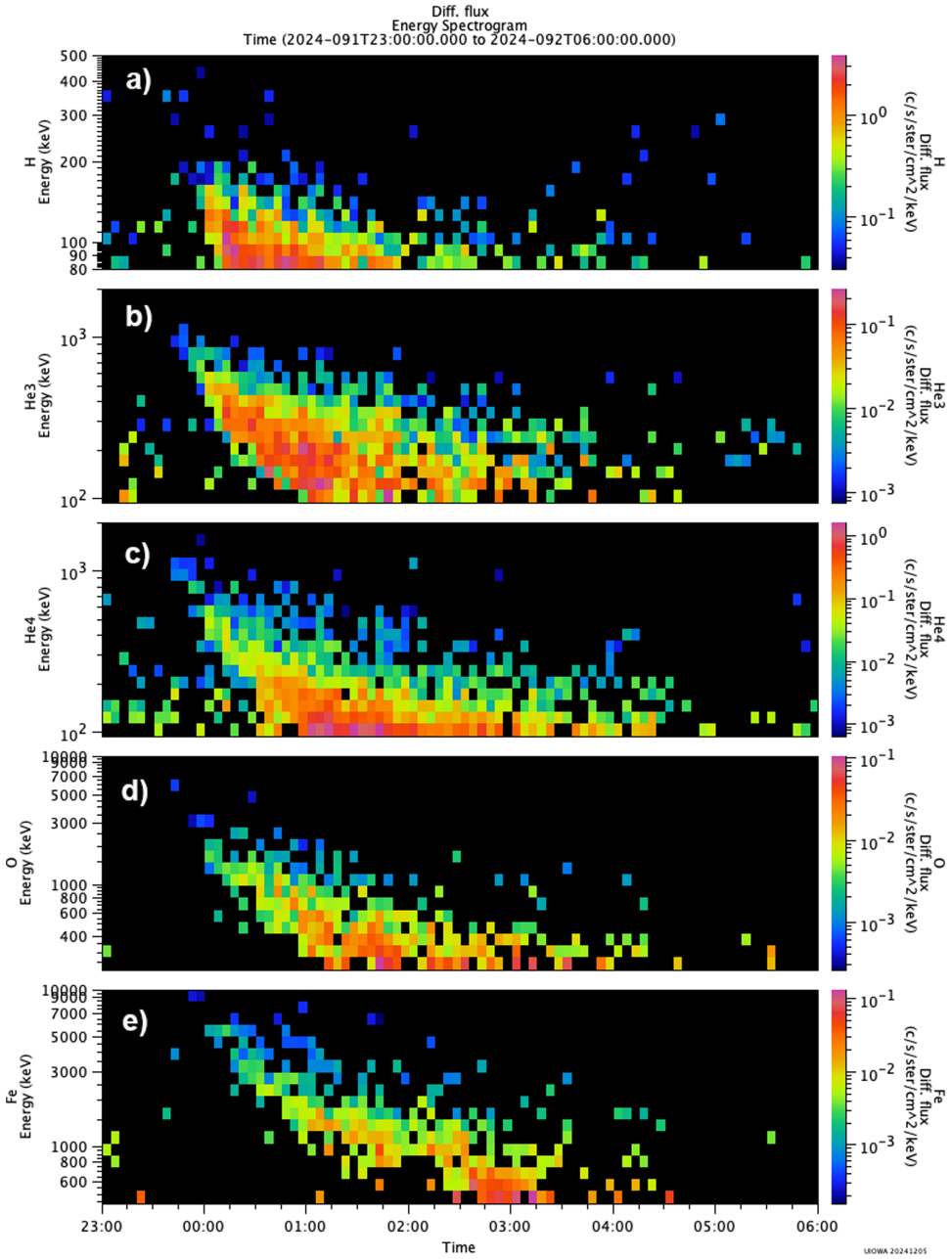

Figure 2. Spectrograms of major species measured by EPI-Lo from 23:00 UT on 2024 March 31 to 06:00 UT on 2024 April 1. (a) hydrogen, (b) ^{3}He, (c) ^{4}He, (d) O, and (e) Fe.

In order to observe clear dispersion of this sort, the spacecraft must be magnetically well connected to the source location of the energetic particles, and the particle transport must be relatively scatter-free. In Section 4, we return to the time dispersion, and in Section 5 to the identification of the solar coronal emissions. In Section 3, we focus on the ^{3}He abundance and the event energy spectral shapes of the primary species.

3. Composition and Energy Spectra

In Figure 2, we showed the energy spectrograms for each of the major species measured by EPI-Lo during the event. In Figure 3, we present the energy-integrated counts of individual particles sampled and telemetered between the event onset at about 23:40 UT on March 31 and 06:00 UT on April 1. The factor of 3 greater abundance of ^{3}He relative to ^{4}He represents the highest observed over this energy range (i.e., by the EPI-Lo instrument) since the launch of PSP in 2018. For most SEP events measured by EPI-Lo, this ratio is <0.03, which is near the lower limit of EPI-Lo's measurement capability for ^{3}He/^{4}He.

Figure 4 presents the event-integrated energy spectra: panel (a) shows the dependence on energy per charge (keV q^{-1}), and panel (b) shows the dependence on energy per nucleon (keV amu^{-1}). In both representations, the spectral shapes are well approximated by power laws for protons and ^{4}He, and by exponentials for ^{3}He, O, and Fe. For each species, the choice between a power law and an exponential was based on which model resulted in a higher correlation coefficient R^2 (shown on the plot). Hydrogen could be fit well with either choice;

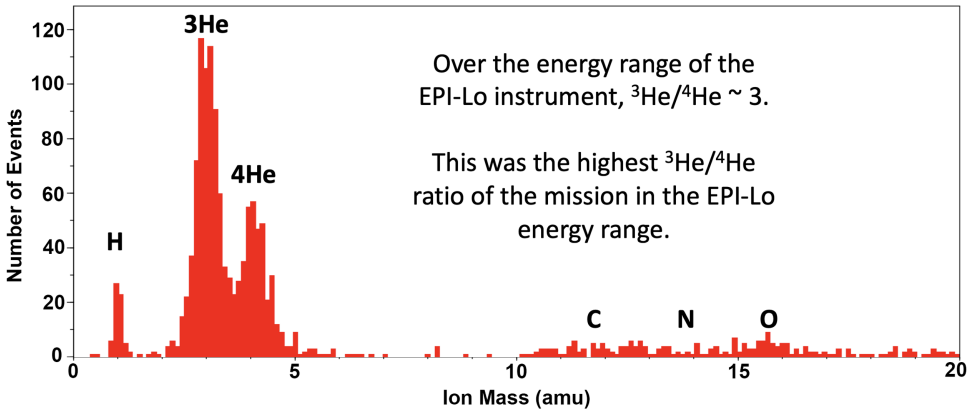

Figure 3. Histogram of species abundances over the energy range 40–250 keV nucleon^{-1}. The hydrogen peak is artificially low, both because there is a priority boundary between H and He in the flight software event-selection process that suppresses the number of protons telemetered, and because the proton spectrum is not sampled below 80keV, the lower threshold of EPI-Lo for this measurement. ^{3}He and ^{4}He are sampled with equal priority and over the full energy range, thus the observed ∼3:1 ratio of ^{3}He/^{4}He is reliable.

however, given its very different slope, it nevertheless behaves differently from the minor species. In either event, the proton spectral shape differs significantly from that of the other species, including ^{4}He, and we do not have an explanation for this observed difference. In Figure 4(a), the exponential spectra exhibit a similar dependence on energy per charge. In Figure 4(b), O and Fe appear to follow similar forms, whereas the roll-over of the spectrum when plotted against energy/nucleon occurs at considerably different keV amu^{-1} for ^{3}He when compared with the roll-over for O and Fe. This observation leads us to infer that (1) the acceleration mechanisms for H and ^{4}He differ from those for the other ions, leading to power-law spectra for H and ^{4}He, although ^{4}He could be interpreted as belonging to the same population as the minor ions since an exponential fit is nearly as good as a power law (whereas the acceleration mechanism for ^{3}He, O, and Fe, as well as arguably ^{4}He, results in exponential spectra); and (2) the ordering of the exponential spectra by energy per charge most simply suggests a mechanism that depends on energy per charge (as opposed to a velocity-dependent mechanism, which would instead result in ordering by energy per nucleon).

Wave–particle interactions can clearly accelerate ions, with wave frequencies that resonate with the ion gyrofrequency (proportional to its charge-to-mass ratio). We expand on this subject below, after first introducing some of the other features associated with this event.

4. Acceleration Profile and Velocity Dispersion

Our understanding of the particle acceleration mechanisms in this event is informed by the spectral shapes (Figure 4), the identification of any activity in the low corona that may be responsible for the abrupt injection or energization of particles (discussed in Section 5), and the time history of the acceleration as determined by the time profile of the event relative to the first-arriving particles for each species. In Figure 5, we present energy spectrograms for hydrogen, ^{3}He, and ^{4}He; time profiles for each species over a common velocity range; and a graphical analysis of particle propagation for each species.

The left three panels in Figure 5 show similar, but not identical, time profiles for the three species. In particular, the ^{3}He profile exhibits elevated count rates over a broader time interval relative to the leading edge than either ^{4}He or H, especially at higher energies (O and Fe statistics do not support a good comparison). To examine this behavior more quantitatively, the middle three panels present line plots of the time profiles over a relatively narrow fixed energy-per-nucleon range (100–130 keV amu^{-1}). This range is chosen to be common to all three species and sufficiently above the EPI-Lo low-energy threshold to provide a good signal-to-noise ratio. In this energy band, both ^{4}He and H exhibit a sharp rise to a narrow peak that is well aligned in time. The ^{3}He profile also rises sharply to a peak, but then remains near its maximum for an additional four data points (∼20 minutes). Since the propagation of these particles from the corona appears to be nearly scatter-free (as evidenced by the very clean dispersion in the antisunward dominated count rates), the observed widths (FWHM $\leqslant$ 10 minutes for H and ^{4}He, ∼25 minutes for ^{3}He) likely reflect the length of time over which each ion species is energized and/or confined in the source region. The vertical blue line shows that the rise above background begins ∼5 minutes earlier for H and ^{4}He than for ^{3}He, suggesting a slight delay in the ^{3}He energization and/or additional confinement in the source region.

In panels (g)–(i), we follow the standard approach of plotting the data (counts in this case, so the reader can assess the statistical significance of the data) binned by $1/\sqrt{\text{energy per nucleon}}$, a quantity proportional to 1/velocity. Extrapolation of this line to zero (i.e., infinite velocity) provides an estimate of the particle injection time in the low corona. The blue diagonal line was fit (by eye) to the ^{4}He data, for which the dispersion is clearest. The same line was then overlain on the H and ^{3}He data. To within the 5 minute resolution of the time binning, the H distribution lies along the same line (indicating a common injection time) as the ^{4}He data. In contrast, the ^{3}He data lie along a bit of a curve, with its closest proximity to the blue dispersion line occurring near 0.1 on the vertical axis, corresponding to an energy of 300 keV (or 100 keV nucleon^{-1}). At this energy, the event-integrated ^{3}He intensity considerably exceeds that of ^{4}He (Figure 3(b)), suggesting strongly preferential acceleration of ^{3}He in this range. The curvature of the leading edge for ^{3}He, lying further from the dispersion line at both higher and lower inverse velocities than at intermediate values, suggests that either the energization above and below that energy range is delayed, the ^{3}He was confined in the low corona longer at those energies, or

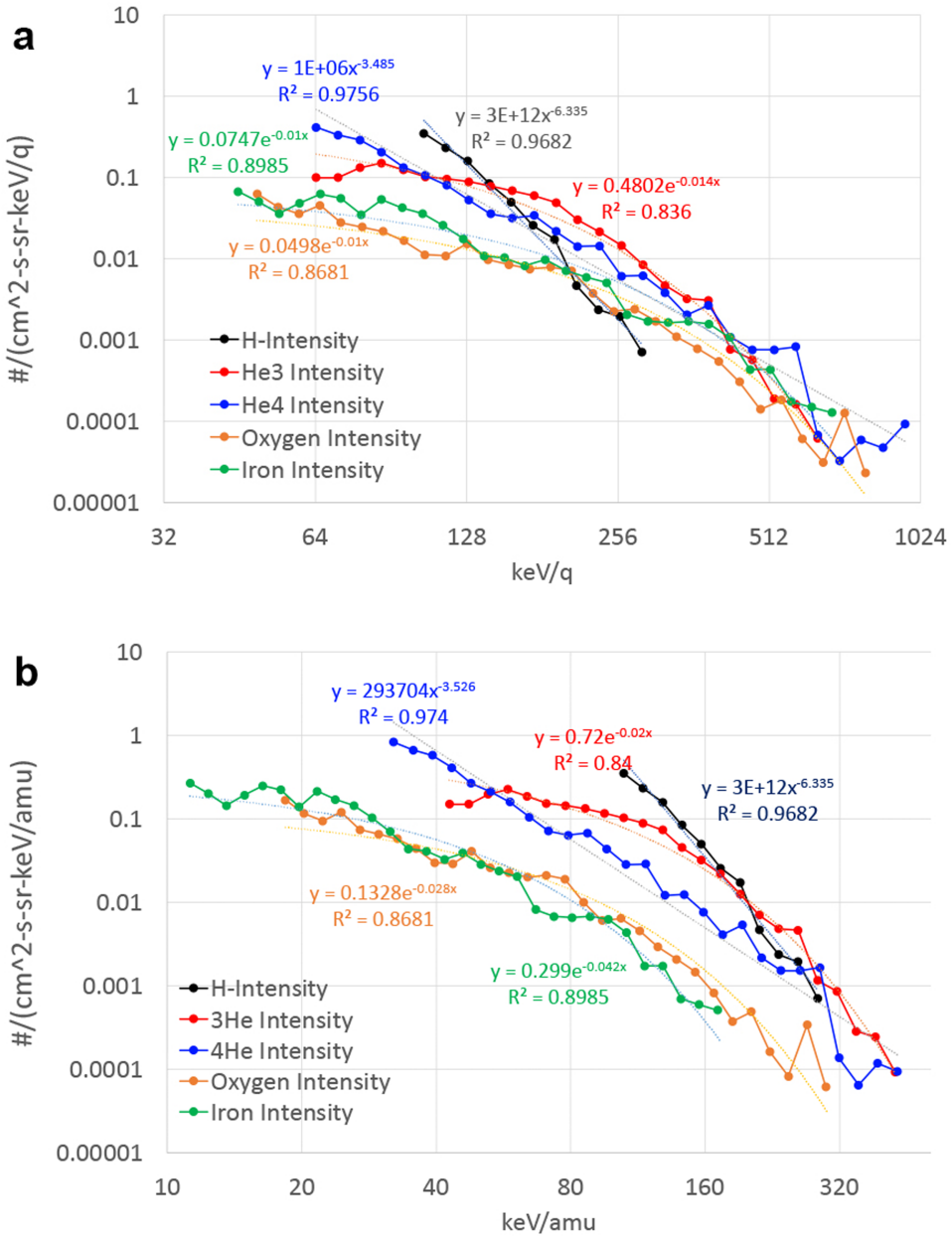

Figure 4. EPI-Lo species spectra, time-integrated over the event. (a) Spectra expressed in energy per charge (keV q^{-1}), using assumed charge states of 1 for H, 2 for He, 6 for O, and 14 for Fe. While different charge-state assumptions for O and Fe are possible, reasonable variations do not significantly affect the relative appearance. (b) Spectra expressed in energy per nucleon (keV amu^{-1}), which is the conventional representation used in most SEP analyses; we show it here for comparison.

that the intensities above and below that range were below the EPI-Lo sensitivity for those early times in the injection. While such scenarios could be attributed to diffusive processes in the source region, we favor a scenario involving a highly efficient yet delayed acceleration process, which can explain both the delayed profile and the enhanced ^{3}He abundance; diffusion alone does not naturally explain the enhanced abundance.

5. Contextual Data, Mapping to the Corona

Broadening our analysis to include additional datasets associated with this event, we searched for other energetic charged particles as well as photon emissions (radio, EUV, and X-ray) that may have been produced. In Figure 6, we plot five datasets: hard X-rays from the Solar Orbiter Spectrometer Telescope for Imaging X-rays (STIX; S. Krucker et al. 2020) in panel (a); type III radio emission as seen by PSP/FIELDS in panel (b) (M. Pulupa et al. 2017); energetic electrons measured by EPI-Lo in its most sunward-facing apertures in panel (c); suprathermal electrons measured by the Solar Wind Electron Alpha Proton instrument (SWEAP; J. C. Kasper et al. 2016) in panel (d); and ^{4}He as measured by EPI-Lo in panel (e). It should be noted that although the onset times (mapped back to the Sun's surface using the propagation speed and assuming direct radial transport) are spread over ∼5 minutes, the associated uncertainties are such that the onsets are consistent with simultaneity within those uncertainties. Furthermore, to the extent that the particle travel times are underestimated by assuming purely radial transport (one could also assume a Parker spiral for the path, which at this distance introduces

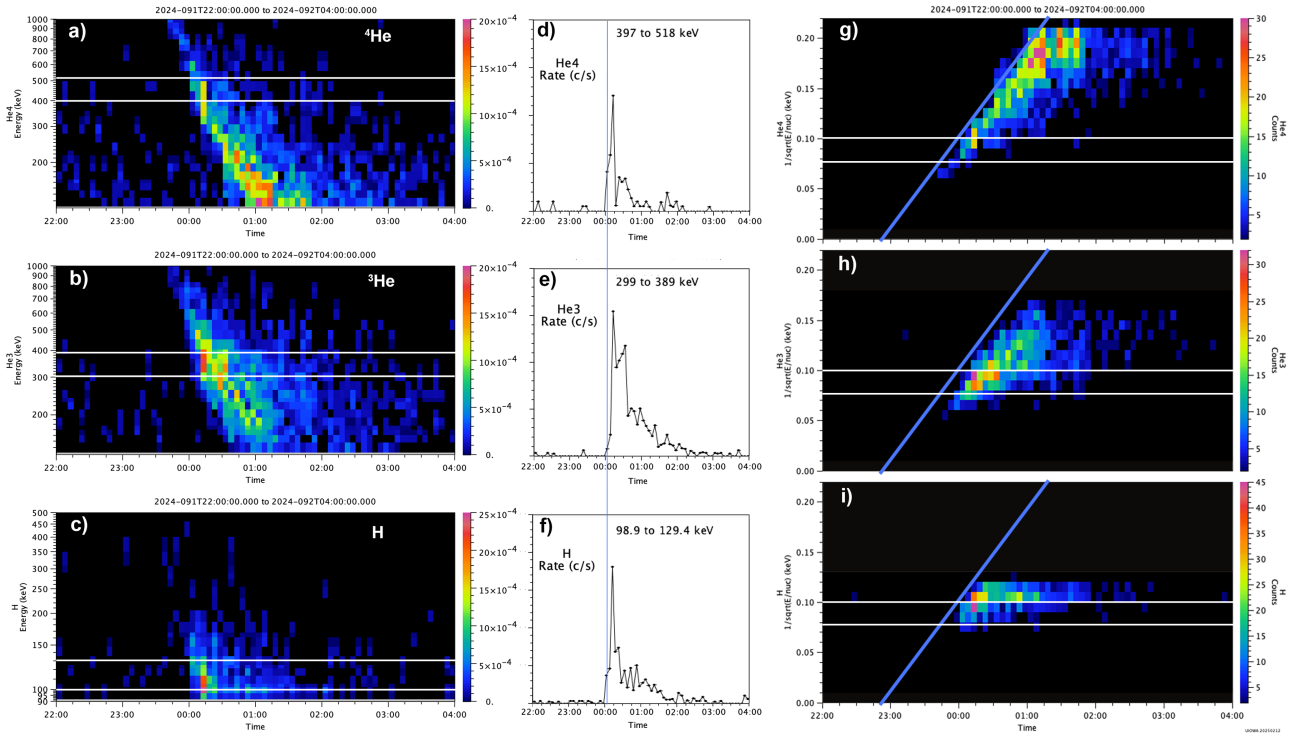

Figure 5. (a)–(c) Energy spectrograms (in counts s^{-1}) for ^{4}He, ^{3}He, and H, respectively, binned at 5 minute resolution. Counts s^{-1} are used to limit the dynamic range in the color bar for improved visibility. Horizontal integrations of the spectrograms over the energy range between the white lines (corresponding to the same energy per nucleon, i.e., velocity for each species) are shown in panels (d)–(f), using the same linear vertical scaling as the color bars for (a)–(c). These profiles show that the ^{3}He distribution remains near its maximum for more than twice as long as the corresponding enhancements in ^{4}He and H. The vertical blue line shows that the onset of the ^{3}He increase is delayed by 5–10 minutes relative to the onset of H and ^{4}He. Panels (g)–(i) show counts for each species vs. the quantity $1/\sqrt{\text{energy per nucleon}}$, which is proportional to 1/velocity. The diagonal blue line represents a fit by eye to the slope of the leading edge of the ^{4}He distribution. The time at which this line intersects the horizontal axis indicates the initial injection time of the event at the Sun. The hydrogen distribution (panel (i)) is in close agreement with this inferred injection time. The ^{3}He distribution appears to lag behind both the H and ^{4}He injection times by ∼10–20 minutes, depending on energy.

only a small difference of order ∼1%), for a nonradial magnetic field they would be slightly shorter, lining up more closely with the photon times.

There are additional considerations that reinforce the association of all these onsets with a single event on the Sun. For example, the type III event, known to be generated by streaming suprathermal and energetic electrons propagating along open coronal and interplanetary magnetic field (IMF) lines, is accompanied by Langmuir waves detected in the local plasma near PSP at the same time the streaming electrons reach the spacecraft. These Langmuir waves are also generated locally by these streaming electrons, supporting a common source for the type III, energetic electrons, and suprathermal plasma electrons. The ion time dispersion yields a source injection time consistent with that of the electrons and the type III burst, within the measurement uncertainty (∼+/−5 minutes for the ions). Additionally, ^{3}He-rich impulsive SEPs are well documented as being associated with both hard X-ray bursts and type III events (R. P. Lin 1985).

Having established that all of the phenomena described in this study are likely associated with a single impulsive injection somewhere in the low corona, occurring in a region with open magnetic topology as implied by the prompt arrival of charged particles at PSP, we now attempt to identify the source region. For this purpose, we use imaging from near-Earth spacecraft, STEREO-A, and SO. Of these, SO—combining STIX X-ray observations with EUV imaging from the X-ray the Extreme-Ultraviolet Imager (EUI; P. Rochus et al. 2020)—provides the best view of the likely PSP magnetic connection regions. Imaging from near Earth by the Solar Dynamics Observatory (SDO; W. D. Pesnell et al. 2012), and from the Extreme-Ultraviolet Imager (EUVI; J. P. Wuelser et al. 2004) on STEREO-A helps constrain the event timing, since the SO/EUI instrument imaging had a cadence of 10 minutes during this interval.

The SO/EUI Full-Sun Imager (P. Rochus et al. 2020) produced full-disk images at 17.4 nm wavelength (Figure 7), revealing two small jets in candidate source regions for the particles seen at PSP. With a 10 minute imaging cadence, the first candidate, observed at 22:41 UT (minus the 2.5 minute light-travel time from the Sun to SO), located at 169° longitude and 11° latitude, appears too early. In contrast, the series of closed loops centered near 175° longitude and 13° latitude remains active throughout the interval of interest. The second candidate, observed at 22:51 UT (again corrected by 2.5 minutes) at 218° longitude and −8° latitude, is at about the right time, although the 10 minute cadence limits precision. This latter region is also the locus of the hard X-ray event shown in Figure 6(a), and its identification with the observed jet is further supported in Figure 8.

From this, we might conclude that the second candidate region is the source of the observed particle event. However, there are complications with this association. To further investigate the coronal source location, we examine the magnetic field measured at PSP and compare it with the open-field magnetic topology in the vicinity of each candidate source region.

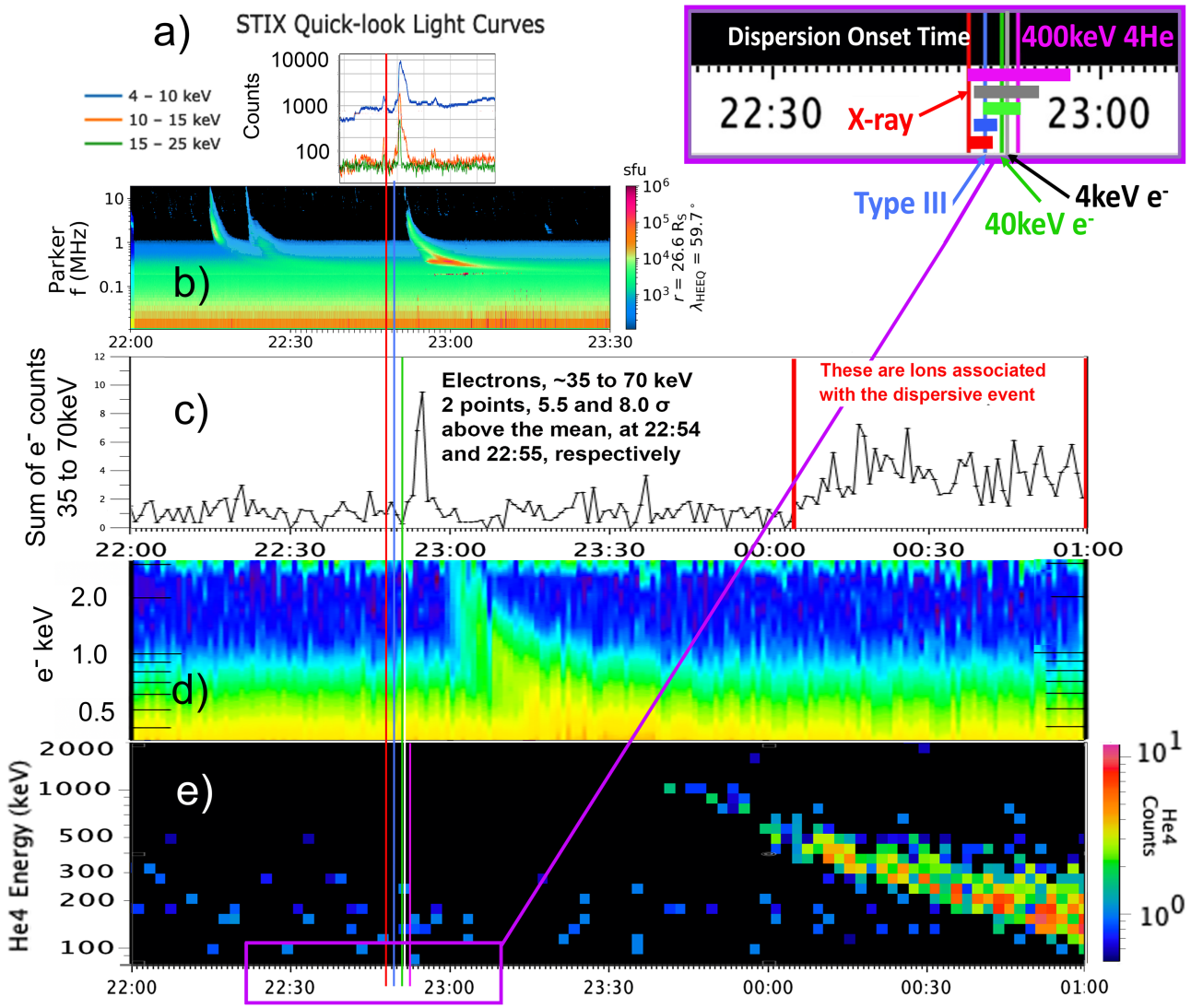

Figure 6. Injection timing for (a) hard X-ray burst as seen from STIX on Solar Orbiter, (b) type III radio emission measured by FIELDS on PSP, (c) energetic electrons detected by EPI-Lo on PSP, (d) suprathermal plasma electrons detected by SWEAP on PSP, and (e) ^{4}He ions detected by EPI-Lo on PSP. Propagating the onset times for each detection back to the Sun (using the radial location of each sensor as an estimate of the distance traveled), we derive the set of colored lines at 22:48:00 UT for the hard X-ray onset, 22:49:30 for the type III, 22:51:00 for the energetic electrons, 22:51:30 for 4 keV plasma electrons, and 22:52:30 for 400 keV ^{4}He ions. The box in the upper right expands the timeline to show the loci of the mapped-back onset times for panels (a)–(e). Horizontal colored bars indicate the estimated uncertainties associated with each mapped-back time. In the X-ray case, this bar shows the width from the rise of the X-ray enhancement. Collectively, these measurements are consistent with a common source in time.

At PSP, the solar wind conditions (Figure 9) are steady, with nearly radially outward magnetic field (B) persisting from more than a day before the event to more than a day afterward. At SO, despite the similar connection point according to the Solar MACH model (Figure 1) and its slightly larger distance from the Sun ($\sim$65 R_s), the solar wind conditions differ substantially from those at PSP. This marked difference in plasma and field conditions at the two probes suggests that despite their nearly identical mapping via the nominal Parker spiral to the high corona, PSP and SO are connected to different sources of solar wind and magnetic field in the low corona. This interpretation is further supported by the fact that the SEP event we have been discussing, seen clearly and unambiguously at PSP, is not seen at all on SO (nor, for that matter, at Earth or STEREO-A, despite their close magnetic connection).

To shed light on these observations, we examine (Figure 10) the mapping of the Parker-spiral footpoints in the high corona to modeled connections with low-coronal source regions for the particles and solar wind. As shown in the table accompanying Figure 1, the high-coronal footpoints for SO and PSP are very close to the same Carrington longitude (CL). From Figure 10, the footpoints are separated by about 4° in latitude, with the PSP high-coronal footpoint located slightly closer to the heliospheric current sheet (HCS), which divides regions of radially outward B at lower Carrington longitude from regions of radially sunward field at higher longitude. The measured magnetic field at SO is consistent with this mapping, as the field varies in angle throughout the period of the event, consistent with a solar wind source near the HCS, where small shifts in footpoint longitude can lead to significant variations in field configuration. From Figure 9, we also see that the PSP magnetic field remains steady and consistently directed radially outward. The solar wind at PSP is also steady and faster than that measured at SO. These observations are consistent with the modeled PSP connection lying in the

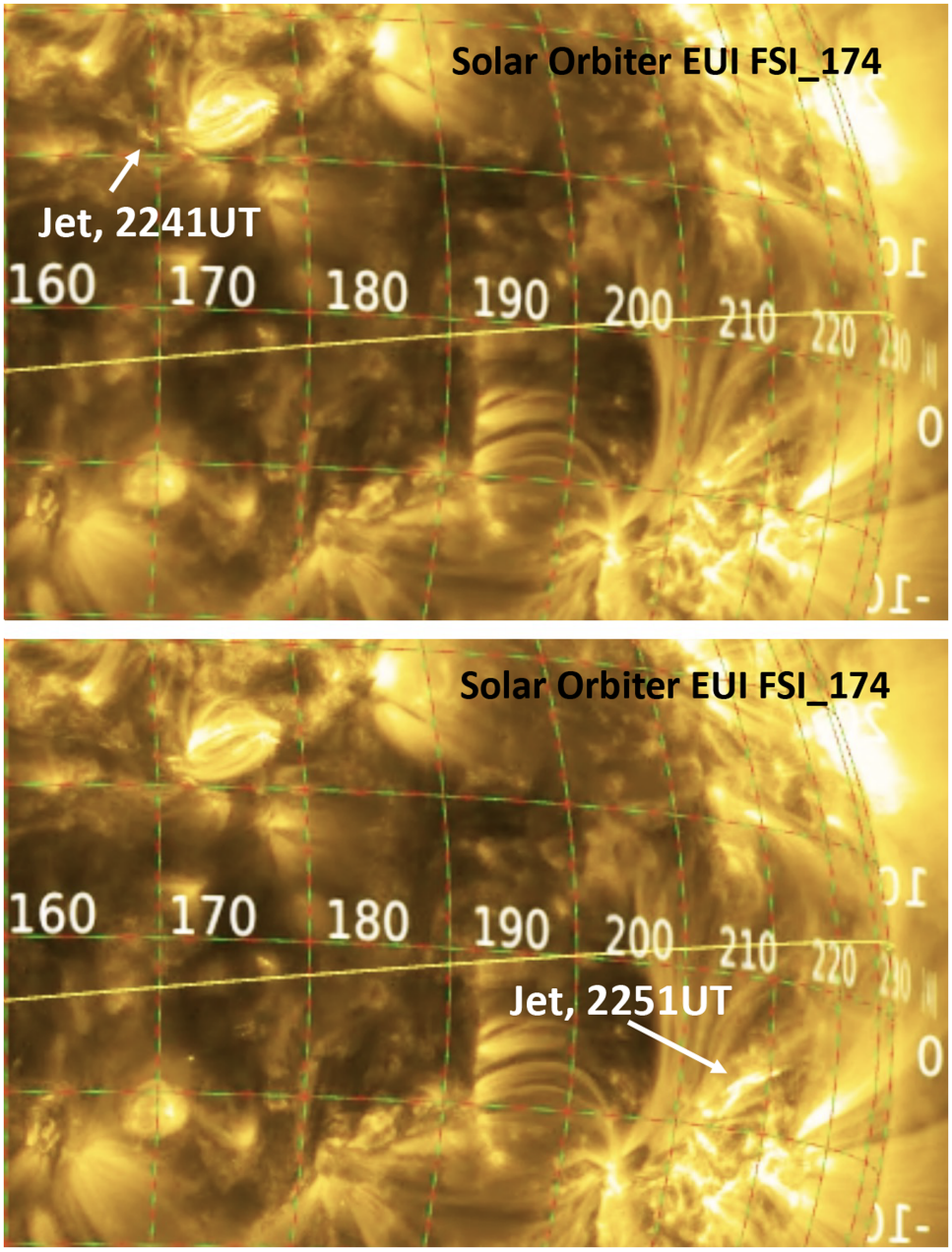

Figure 7. Solar Orbiter EUI FSI 17.4 nm images. Top: 2024 March 31, 22:41 UT. Bottom: 2024 March 31, 22:51 UT. The two dynamic features shown are candidate source regions for the impulsive event seen at PSP.

open-field region to the west of the HCS, between 160° and 170° CL in Figure 10.

6. Discussion and Conclusions

The suggested mapping of the PSP connection to the low corona into the open, radially outward field region centered near 160° CL introduces a complication in associating the observed particle and photon emissions with the coronal jet and X-ray activity centered near 210°. The latter region is the source of the hard X-ray event detected by SO/STIX, whose timing coincides very closely with the derived injection time of the particles and the type III radio emission. The jet observed by SO/EUI (Figures 7 and 8) in the same region is also the most prominent jet observed that is temporally consistent candidate for the observed injection phenomena. However, none of the particle signatures are observed at SO, despite its nominally better connection with this activity than PSP. Additionally, PSP measures a magnetic field polarity consistent with connection to the coronal open-field region near 160° longitude.

This raises the question of whether the particles measured by EPI-Lo (energetic ions and 35–70 keV electrons) and SWEAP (1–4 keV electrons), as shown in Figure 6, originate from coronal activity near 210° and subsequently "hop" through closed field into the open-field region near 160°, where they then move (via reconnection or diffusion) onto adjacent open field lines and propagate outward to PSP; or whether they originate in activity near the open-field region at ∼160° CL and escape directly to PSP, and are therefore unrelated to the hard X-ray event and jet at ∼210°.

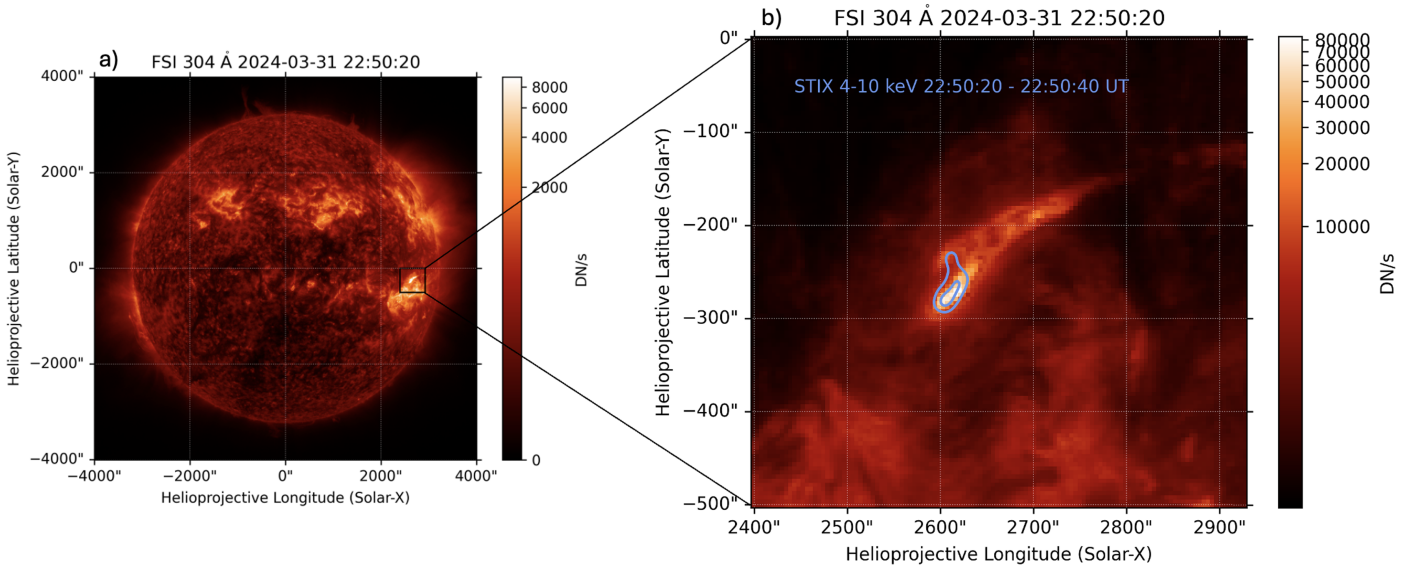

Figure 8. (a) Solar Orbiter EUI FSI 30.4 nm image at 2024 March 31, 22:50 UT, showing a small jet that is saturated. (b) Calibrated flux of the same jet, with STIX 4–10 keV contours overplotted, identifying the jet as the source of the hard X-ray burst.

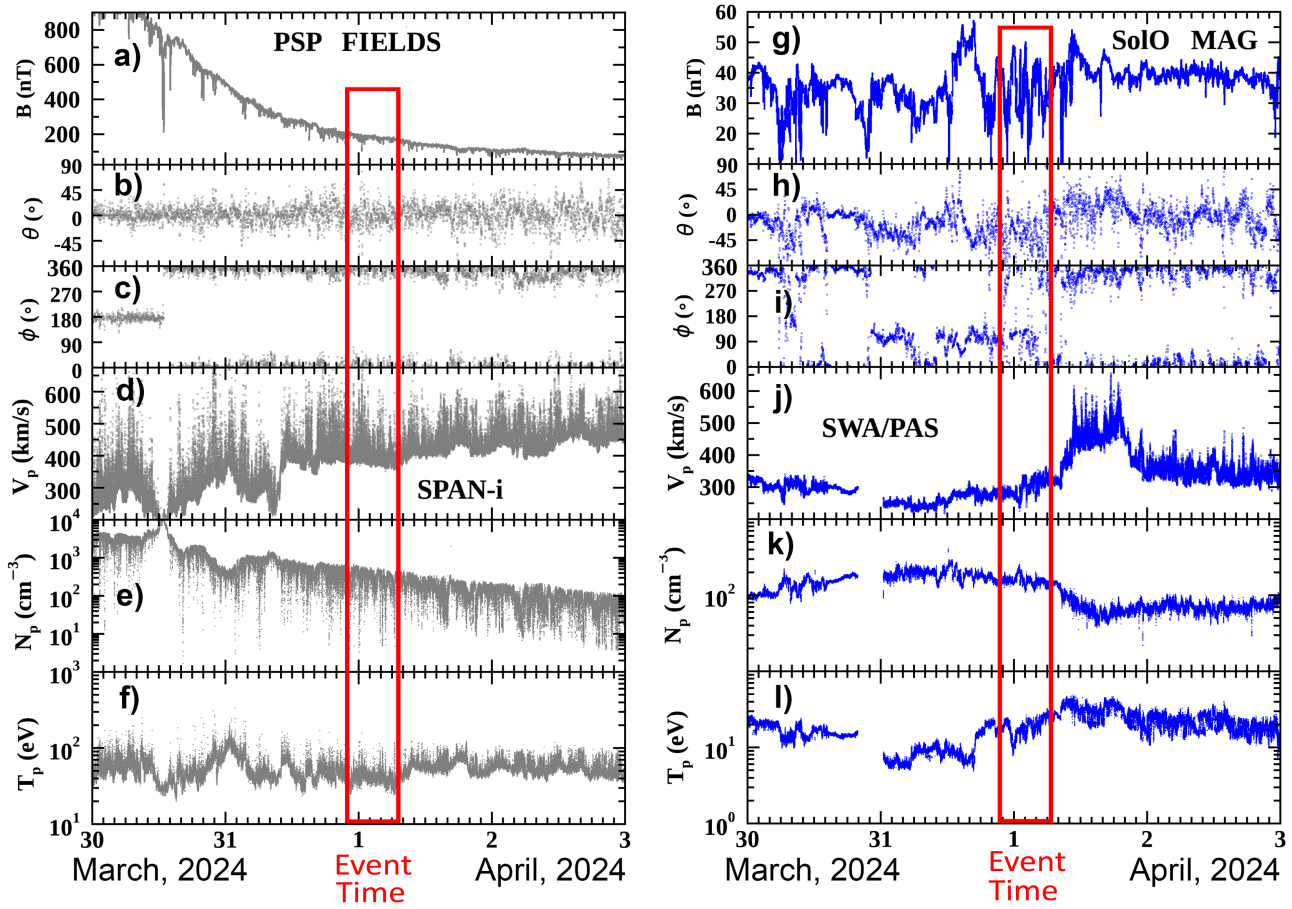

Figure 9. PSP and Solar Orbiter (SolO) magnetic field and plasma moments during the time period 2024 March 30–April 3. (a)–(f) PSP; (g)–(l) SolO. The time bounds for the impulsive event seen at PSP are indicated by the red rectangles.

Arguments can be made for both scenarios. We therefore leave the issue open: Either the PSP event and type III radio emission are associated with the very small jet and active loop structure observed near 170° CL (Figure 7, top), for which the IMF polarity measured at PSP agrees; or they are associated with. the better-timed X-ray event and jet observed near 210° (Figure 7, bottom, and Figure 8), for which the polarity of the IMF at PSP requires low-coronal transport of particle populations across ∼40° in longitude. Based on the IMF polarity, we surmise that the electrons that reach PSP must travel along open field rooted in the radially outward field region near 160° longitude. Since the type III emission is

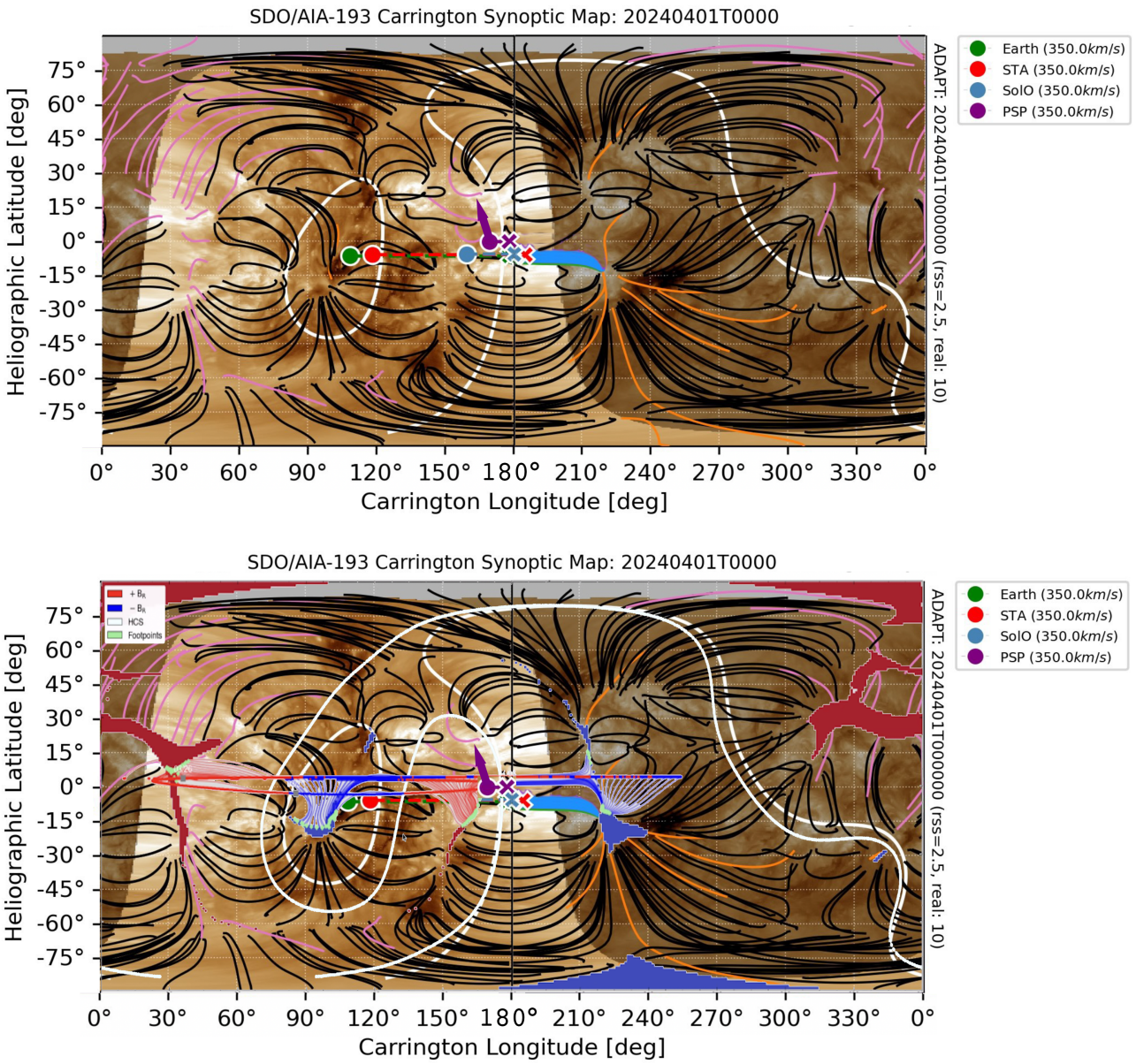

Figure 10. Top: mapping of Earth, STEREO-A (STA), Solar Orbiter (SolO), and PSP to high-coronal footpoints at the assumed 2.5 R_s source surface (colored ×'s based on Solar MACH). The blue swath extending from the blue × (SolO) indicates the estimated mapping into the low corona at the time of event onset. Black lines represent closed field within the 2.5 R_s boundary assumed by the model for the high-coronal mapping. Pink (orange) lines represent field lines that cross the 2.5 R_s boundary and have inward (outward) radial components, respectively. The loci of the HCS is shown in white. Bottom: same plot, with estimated PSP low-coronal connections (red indicates antisunward radial component of B; blue indicates sunward). Two slightly different HCS loci are overlain in the panel as they were derived at slightly different times (the first was at the time of the event shown in the top panel, and the second at PSP perihelion). Note that the HCS location is effectively identical in the vicinity of the PSP-mapped connection location and is therefore insensitive to the epoch used. Estimated PSP low-coronal footprints are shown in light green.

driven by streaming electrons, it must also be tied to either a direct or indirect (along closed loops from ∼210° longitude) source of the energetic electrons in that open-field region. By the same argument, the energetic ions must also originate within the open-field region at 160° CL connected to PSP.

The strong enhancement of ^{3}He in the event and exponential spectral shapes for ^{3}He, O, and Fe support a wave–particle acceleration process affecting minor ions. The waves required to accelerate the minor ions are thought to be generated by the electron beams streaming along open field lines. Another characteristic linking the ^{3}He acceleration to the waves generated by electrons escaping along open field is the temporal width of the ^{3}He injection (as shown in Figure 5(e)), indicating a more extended acceleration phase than that for protons and ^{4}He (Figures 5(d) and (f)), consistent with the ∼30 minute width of the elevated suprathermal electron flux (Figure 6(d)). Likewise, the delayed rise of the ^{3}He intensities (by at least 5 minutes relative to the onsets of ^{4}He and protons at ∼100 keV nucleon^{-1}, and longer at lower and higher energies) suggests an acceleration mechanism that is distinct from that responsible for the ^{4}He and H, presumably a wave–particle mechanism.

We therefore conclude that the ions are generated in the open-field region with radially outward B field, regardless of whether the electron population hops from the region at 210° longitude or not.

In D. G. Mitchell et al. (2020), we proposed that ion heating and acceleration in small impulsive events may operate via a mechanism analogous to the "pressure cooker" mechanism in auroral physics (C. W. Carlson et al. 1998, R. E. Ergun et al. 1998; D. M. Klumpar 1990; E. J. Lund et al. 2001; G. T. Marklund et al. 2001; K. A. Lynch et al. 2002). If the same mechanism is operating in this event, we would expect the energization of all the minor ion species to be ordered by energy per charge, resulting in the common spectral energy-per-charge dependence observed in Figure 4(a) (the energy reached in the pressure cooker mechanism is more a function of the confining electric field than it is of the wave-heating growth time constant). However, a twist on that story was suggested by G. M. Mason et al. (2023), who argue that because of the much higher contributions to plasma density by H and ^{4}He in the wave-heating region in the low corona, the wave power at the gyrofrequencies of those constituents is significantly damped, such that they are not effectively heated by the wave field. In that case, the acceleration of H and ^{4}He is dominated not by the pressure cooker mechanism, but rather presumably by the reconnection process at the open–closed interface responsible for the prompt coronal jet, as well as the H and ^{4}He acceleration (e.g., J. F. Drake et al. 2013). This difference may explain the prompt appearance of H and ^{4}He, with the delay in ^{3}He resulting from a different, slower acceleration mechanism.

Returning to the choices for the low-coronal source, we leave open the possibilities for where the triggering event occurred in the low corona, but argue in either case for the escape of particles into the solar wind in, or adjacent to, the open-field region near 170° CL. The event is only seen at PSP, which is clearly (based on *B*-field polarity) connected with that region; it is not seen at SO, which is more likely connected with the HCS between the open region near 170° and the open-field region near 210° longitude, where the hard X-ray event is observed. If the originating source is in the active region near 210° longitude, the near-simultaneous (within ∼2 minutes) arrival of the energetic electrons, H, and ^{4}He at an IMF injection location connected to the open-field region near 170° argues for a transport process in the low corona that moves particles from the radially inward-directed *B*-field region near 210° longitude, across the HCS, and into the radially outward open-field region near 170°, where PSP is magnetically connected. Such a sequence would require a prompt, energy- and rigidity-independent cross-field diffusion process capable of transporting at least protons, ^{4}He ions, and electrons along such a path through the lower corona.

Acknowledgments

Parker Solar Probe was designed, built, and is operated by the Johns Hopkins Applied Physics Laboratory as part of NASA's Living with a Star (LWS) program (contract NNN06AA01C). Support from the LWS management and technical team has played a critical role in the success of the Parker Solar Probe mission.

This work was supported by the IS⊙IS instrument suite on NASA's Parker Solar Probe Mission, contract NNN06AA01C. The data supporting the analysis of the energetic-particle event was measured largely by the EPI-Lo instrument of the IS⊙IS instrument suite. P.M. acknowledges the support from NASA HGIO grant No. 80NSSC23K0419. G.M.M. also acknowledges support under NASA contract NNN06AA01C. D.L. acknowledges support from the Strategic Capability project under NASA grant No. 80NSSC22K0892 (SCEPTER).

ORCID iDs

D. G. Mitchell https://orcid.org/0000-0003-1960-2119
D. Lario https://orcid.org/0000-0002-3176-8704
G. M. Mason https://orcid.org/0000-0003-2169-9618
A. Kouloumvakos https://orcid.org/0000-0001-6589-4509
G. Berland https://orcid.org/0000-0001-6010-6374
D. J. McComas https://orcid.org/0000-0001-6160-1158
C. M. S. Cohen https://orcid.org/0000-0002-0978-8127
M. E. Hill https://orcid.org/0000-0002-5674-4936
R. L. McNutt, Jr https://orcid.org/0000-0002-4722-9166
P. S. Mostafavi https://orcid.org/0000-0002-3808-3580
J. C. Kasper https://orcid.org/0000-0002-7077-930X
S. D. Bale https://orcid.org/0000-0002-1989-3596
M. Pulupa https://orcid.org/0000-0002-1573-7457
P. L. Whittlesey https://orcid.org/0000-0002-7287-5098

References

Bale, S. D., Drake, J. F., McManus, M. D., et al. 2023, Natur, 618, 252
Carlson, C. W., McFadden, J. P., Ergun, R. E., et al. 1998, GeoRL, 25, 2017
Desai, M. I., Mason, G. M., Dwyer, J. R., et al. 2003, ApJ, 588, 1149
Drake, J. F., Swisdak, M., & Fermo, R. 2013, ApJL, 763, L5
Ergun, R. E., Carlson, C. W., McFadden, J. P., et al. 1998, GeoRL, 25, 2025
Gieseler, J., Dresing, N., Palmroos, C., et al. 2023, FrASS, 9, 384
Hill, M. E., Mitchell, D. G., Andrews, G. B., et al. 2017, JGRA, 122, 1513
Kasper, J. C., Abiad, R., Austin, G., et al. 2016, SSRv, 204, 131
Klumpar, D. M. 1990, in Physics of Space Plasmas, ed. T. Chang et al. (AGU), 265
Krucker, S., Hurford, G. J., Grimm, O., et al. 2020, A&A, 642, A15
Lin, R. P. 1985, SoPh, 100, 537
Mason, G. M., Reames, D. V., Klecker, B., & Hovestadt, D. 1986, ApJ, 303, 849
Mason, G. M., Wiedenbeck, M. E., Miller, J. A., et al. 2002, ApJ, 574, 1039
Mason, G. M., Nitta, N. V., Cohen, C. M. S., & Wiedenbeck, M. E. 2009, ApJ, 700, L56
Mason, G. M., Roth, I., Nitta, N. V., et al. 2023, ApJ, 957, 112
McComas, D. J., Alexander, N., Angold, N., et al. 2016, SSRv, 204, 187
Mitchell, D. G., Giacalone, J., Allen, R. C., et al. 2020, ApJS, 246, 59
Mitchell, D. G., Hill, M. E., McComas, D. J., Cohen, C. M. S., et al. 2024, ApJ, 965, 54
Lund, E. J., Möbius, E., Lynch, K. A., et al. 2001, PCEC, 26, 161
Lynch, K. A., Bonnell, J., Carlson, C., & Peria, W. 2002, JGRA, 107, 1115
Marklund, G. T., Ivchenko, N., Karlsson, T., et al. 2001, Natur, 414, 724
Pesnell, W. D., Thompson, B. J., & Chamberlin, P. C. 2012, SoPh, 275, 3
Pulupa, M., Bale, S. D., Bonnell, J. W., et al. 2017, JGRA, 122, 2836
Raouafi, N. E., & Stenborg, G. 2014, ApJ, 787, 118
Raouafi, N. E., Stenborg, G., Seaton, D. B., et al. 2023, ApJ, 945, 28
Reames, D. V. 2015, SSRv, 194, 303
Reames, D. V. 1999, SSRv, 90, 413
Reames, D. V. 2024, FrASS, 11, 1368043
Rochus, P., Auchère, F., Berghmans, D., et al. 2020, A&A, 642, A8
Roth, I., & Temerin, M. 1997, ApJ, 477, 940È957
Schwadron, N. A., Lee, M. A., Gorby, M., et al. 2015, ApJ, 810, 97
Temerin, M., & Roth, I. 1992, ApJL, 391, L105
Wuelser, J. P., Lemen, J. R., Tarbell, et al. 2004, SPIE, 5171, 111
Zharkova, V. V., Arzner, K., Benz, A. O., et al. 2011, SSRv, 159, 357